Oxygen Isotope Ratios in Hydrogen-Deficient Carbon Stars: Insights into Low-Mass White Dwarf Merger outcomes

Advait Mehla,[1] Mansi M. Kasliwal,[2] Viraj Karambelkar,[2] Patrick Tisserand,[3] Courtney Crawford,[4] Geoffrey Clayton,[5] Jamie Soon,[6] and Varun Bhalerao[1]

[1] Department of Physics, Indian Institute of Technology Bombay, Powai 400076, India

[2] Division of Physics, Mathematics, and Astronomy, California Institute of Technology, Pasadena, CA 91125, USA

[3] Sorbonne Universités, UPMC Univ. Paris 6 et CNRS, UMR 7095, Institut d'Astrophysique de Paris, IAP, 75014 Paris, France

[4] Sydney Institute for Astronomy (SIfA), School of Physics, University of Sydney, NSW 2006, Australia

[5] Space Science Institute, 4765 Walnut St, Suite B, Boulder, CO 80301, USA

[6] Research School of Astronomy and Astrophysics, Australian National University, Cotter Rd, Weston Creek ACT 2611, Australia

ABSTRACT

Hydrogen-deficient Carbon (HdC) stars are a class of supergiants with anomalous chemical compositions, suggesting that they are remnants of CO-He white dwarf (WD) mergers. This class comprises two spectroscopically similar subclasses – dusty R Coronae Borealis (RCB) and dustless Hydrogen-deficient Carbon (dLHdC) stars. Both subclasses have a stark overabundance of ^{18}O in their atmospheres, but spectroscopic differences between them remain poorly studied. We present high-resolution ($R \approx 75000$) K-band spectra of six RCB and six dLHdC stars, including four newly discovered dLHdC stars, making this the largest sample to date. We develop a semi-automated fitting routine to measure $^{16}O/^{18}O$ ratios for this sample, tripling the number of dLHdC stars with oxygen isotope ratios measured from high resolution spectra. All six dLHdC stars have $^{16}O/^{18}O < 1$, while the RCB stars have $^{16}O/^{18}O > 4$. Additionally, for the first time, we find a trend of decreasing $^{16}O/^{18}O$ ratios with increasing effective temperature for HdC stars, consistent with recent model predictions. Our results affirm the emerging picture that mass ratio/total mass of the WD binary determines whether an RCB or dLHdC is formed post merger. However, we note that current models overpredict the low $^{16}O/^{18}O$ ratios of dLHdC stars by two orders of magnitude. We also measure abundances of C, N, O, Fe, S, Si, Mg, Na, and Ca for the six RCB and six dLHdC stars. We observe a correlation between the abundances of ^{14}N and ^{18}O in our sample which implies that a fixed fraction of the ^{14}N is converted to ^{18}O in these stars via α-capture on ^{14}N.

1. INTRODUCTION

Hydrogen-deficient Carbon (HdC) stars are a class of supergiant stars with unusual chemical compositions, characterized by an acute deficiency of hydrogen and an overabundance of carbon (Clayton 1996, 2012; Lambert & Rao 1994). Their peculiar chemical compositions suggest that they originate in the merger of a CO-core and an He-core white dwarf (Clayton et al. 2007) in what is known as the double-degenerate (DD) formation scenario. They are found in all old galactic substructures, the thick disk, the bulge and the halo, but also the younger one, i.e., the thin disk (Tisserand et al. 2024). Adding to their intrigue, HdC stars seem to comprise two varieties with similar chemical compositions but distinct photometric properties: R Coronae Borealis (RCB)-type stars that show erratic brightness variations resulting from dust ejection episodes (Tisserand et al. 2020), and dustless Hydrogen-deficient Carbon (dLHdC) stars that do not show dramatic bright-

ness variations or any signs of dust formation (Tisserand et al. 2022). Why RCB stars form dust while dLHdC stars do not despite having similar chemical compositions is still a mystery.

Several studies have attempted to identify chemical differences between RCBs and dLHdC stars as a step towards solving their dusty mystery. Using medium resolution K-band spectra of these stars covering the CO molecular absorption bandheads, Clayton et al. (2007) first noted that RCB stars and dLHdC stars possibly differ in their oxygen isotope ratios, with dLHdCs having $^{16}O/^{18}O < 1$, while RCBs having $^{16}O/^{18}O > 1$. This was confirmed with high-resolution spectra by García-Hernández et al. (2009, 2010). However, these studies were based on small samples of five RCB stars and two dLHdC stars. Although there were over fifty RCB stars known at the time, only four dLHdC stars were known, of which two were too warm to exhibit CO lines. However, this has changed recently with the discovery of 27

new dLHdC stars (Tisserand et al. 2022). Additionally, a large number of RCB stars have been observed at near-infrared wavelengths (Karambelkar et al. 2021, 2024), enabling spectroscopic comparisons of larger samples of RCB and dLHdC stars.

Using medium resolution NIR spectra for the expanded sample of RCBs and dLHdCs, (Karambelkar et al. 2022) showed that dLHdC stars generally tend to have lower values of $^{16}O/^{18}O$ than RCBs, and suggested that this difference could be attributed to different masses or mass-ratios of the merging white-dwarfs Crawford et al. (2024). However, the oxygen isotope ratios measured from the medium resolution spectra have large uncertainties due to excessive blending with molecular CN lines in this wavelength range. This lack of precision precludes any further insights, such as quantitative comparisons with theoretical models or identification of trends within the data.

In this paper, we present high resolution (R≈75000) K-band spectra of six RCB and six dLHdC stars. These spectra are the highest resolution NIR specta of the largest sample of RCB and dLHdC stars to date. We use these spectra to derive the oxygen isotope ratios and other elemental abundances of these stars and examine differences between RCB and dLHdC stars. The paper is structured as follows - Section 2 describes the spectroscopic observations, Section 3 describes the abundance measurement method, 4 examines the differences and trends of the abundance measurements. We conclude with a summary of our results in Section 5.

2. OBSERVATIONS

Our data consists of high-resolution ($R \approx 75000$ or 4 km/s) K-band spectra of nine RCB and six dLHdC stars acquired with the iSHELL spectrograph (Rayner et al. 2022) on the 3.2 m NASA Infrared Telescope Facility (IRTF) at Mauna Kea Observatory, Hawaii. The observations were obtained over six nights between 2022 September 14 and 2022 October 3, with the 0.375" slit, using the K order sorter in the K_3 mode which covers the wavelength range of $2.25 - 2.48$ μm. This region was chosen to include multiple bandheads of $^{12}C^{16}O$ and $^{12}C^{18}O$, as well as several lines of $^{12}C^{14}N$. The full log of observations is listed in Table 1. We reduced the spectra using the `idl` software `spextool` (Cushing et al. 2004), and were calibrated and corrected for telluric absorption using the `xtellcor` package (Vacca et al. 2003). Table 1 also lists the median signal-to-noise ratios for the spectra measured at the continuum level in the $2.3 - 2.4$ μm region, which ranges from 32 to 127.

For the RCB stars in our sample, we determined their photometric phases at the epochs of the IRTF observa-

tions using time-series photometric information aggregated from various surveys by the DREAMS monitoring portal[1]. Of the nine RCB stars, IRAS 1813+ and WISE J1820+ were observed in a decline, where their V-band brightness were fainter by $\Delta V \approx 1$ and $\Delta V \approx 3$ mag than maximum luminosity respectively. Subsequently, the spectra for these two stars have not been analyzed as the photospheric lines are heavily diluted by newly ejected dust clouds. Additionally, although it was observed at maximum light, V CrA was found to have a heavily diluted and featureless spectrum, due to a combination of its high estimated effective temperature (~ 6500 K) and large K-band excess due to circumstellar dust. ASAS-RCB-18 and ASAS-RCB-21 were recovering from decline phases and were both roughly 0.8 mag fainter than maximum luminosity, but this does not appear to appreciably dilute the photospheric spectrum. The remaining four RCB stars were observed at maximum light, bringing the total number of RCB stars analyzed in this work to six.

We note that among our dLHdC stars, Tisserand et al. (2024) reported that four belong to the Bulge structure (A223, B42, C38 and B566), one to the thick disk (HD 137613) and the last one, HD 182040, possibly to the thin disk. Only one of our RCB stars were classified in a galactic sub-substructure: NSV 11154 was given the label of a halo star due to its high position above the galactic plane and high measured radial velocity.

3. ABUNDANCE ANALYSIS

3.1. *Notable Spectral Features*

Our spectra cover several molecular absorption features such as the CN Red System of $^{12}C^{14}N$, the first seven overtone bandheads of $^{12}C^{16}O$, the first five overtones of $^{12}C^{18}O$ (listed in Table 3.1), and C_2 absorption lines from the Phillips and Ballik-Ramsay systems. There is considerable blending of lines especially beyond 2.29 μm. Figure 1 shows a region with prominent CN lines for both dLHdC and RCB stars, along with a CN synthetic spectrum generated for one star in each class. Figure 2 shows a region dominated by $^{12}C^{16}O$ and $^{12}C^{18}O$ lines for the dLHdC and RCB stars. We also have several atomic lines in our spectra, however most of them are severely blended with molecular features. A few prominent ones that we use for recovering elemental abundances are listed in Table 3.1.

Our wavelength range also includes bandheads of $^{13}C^{16}O$, but these are not detected in any star in our sample. This indicates a high $^{12}C/^{13}C$ ratio that is con-

---

[1] https://dreams.anu.edu.au/monitoring/
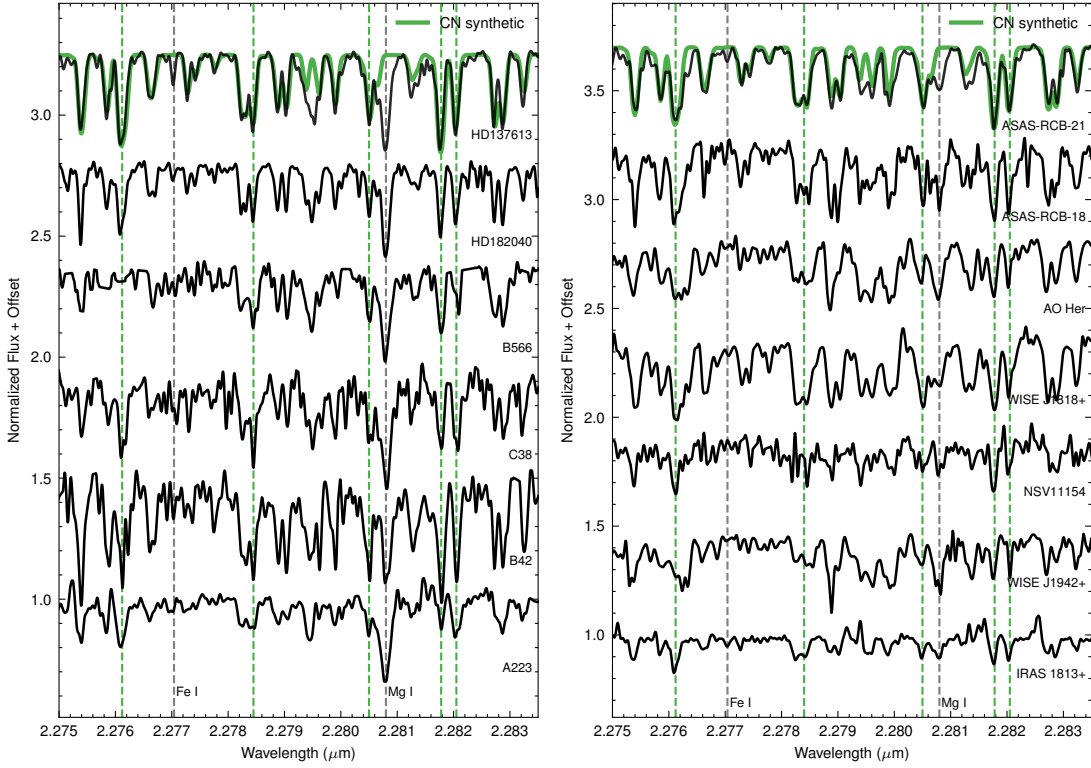
Figure 1. Spectra centred at ∼2.28 μm showing a region with $^{12}C^{14}N$ lines for the dLHdC stars (left) and RCB stars (right). $^{12}C^{14}N$ synthetic spectra generated for HD 137613 and ASAS-RCB-21 are overplotted in green for comparison, with a few strong lines marked. Also marked in gray are the locations of a few atomic lines.
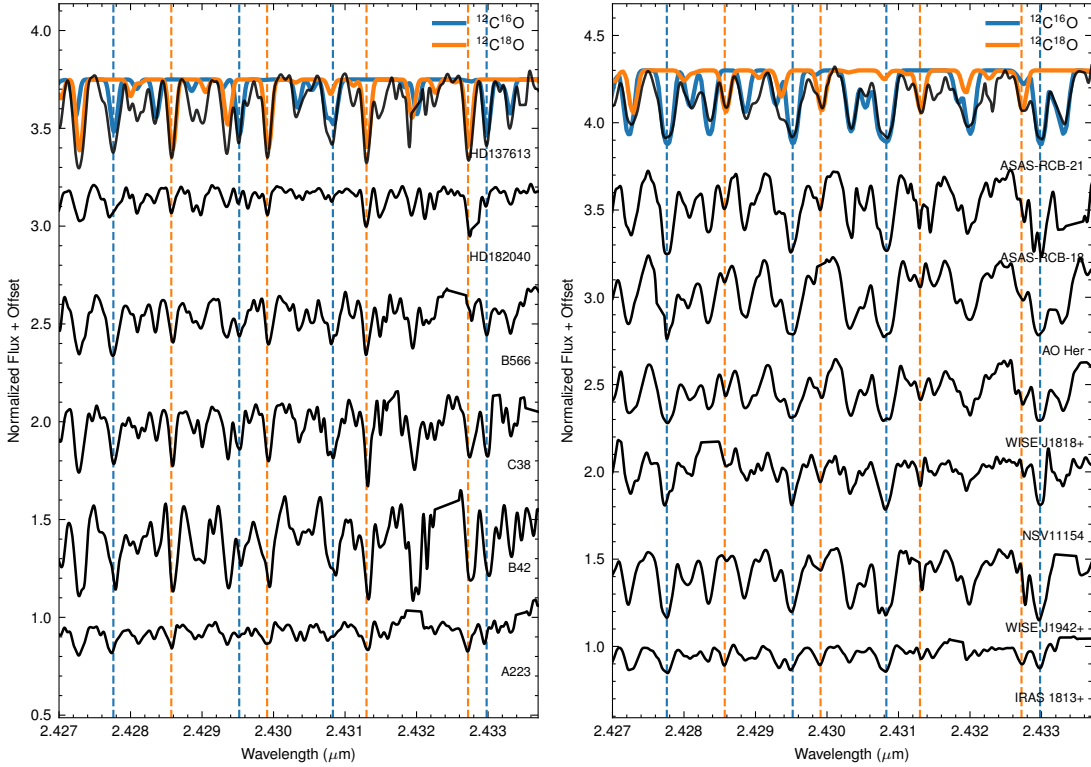

Figure 2. Spectra centred at ∼2.43 μm showing a region dominated by $^{12}C^{16}O$ and $^{12}C^{18}O$ lines for the dLHdC stars (left) and RCB stars (right). Individual synthetic spectra generated for HD 137613 and ASAS-RCB-21 are overplotted in blue and orange for comparison, with a few strong lines marked. It is clear that $^{12}C^{18}O$ is the dominant isotopologue in all dLHdC stars, while $^{12}C^{16}O$ is much more prominent in RCB stars.

Table 1. Log of spectroscopic observations.

Name	Class	Date (UT)	S/N	Telluric Standard	Exposure Time (min)
HD 137613	dLHdC	2022-09-14	104	HIP79881	5.0
A223*	dLHdC	2022-09-14	127	HIP93667	57.5
B42*	dLHdC	2022-09-14	32	HIP93667	20.0
HD 182040	dLHdC	2022-09-22	108	HIP95793	3.0
C38*	dLHdC	2022-09-23	73	HIP93667	100.0
B566*	dLHdC	2022-09-30	78	HIP91137	90.0
WISE J1820+	RCB	2022-09-24	41	HIP93667	24.0
WISE J1942+	RCB	2022-09-22	98	HIP98953	50.0
IRAS 1813+	RCB	2022-09-22	149	HIP95793	50.0
ASAS-RCB-18	RCB	2022-09-23	79	HIP95793	13.5
V CrA	RCB	2022-09-23	136	HIP93470	10.0
AO Her	RCB	2022-09-24	88	HIP91315	10.0
ASAS-RCB-21	RCB	2022-09-24	81	HIP95793	27.0
NSV 11154	RCB	2022-09-24	87	HIP91315	54.0
WISE J1818+	RCB	2022-09-30	68	HIP93667	7.5

Note: The recently discovered dLHdC stars (Tisserand et al. 2022) are marked by asterisks.
The following abbreviations are used throughout the text: WISE J194218.38-203247.5: WISE J1942+; IRAS 1813.5-2419: IRAS 1813+; WISE J181836.38-181732.8: WISE J1818+; WISE J182010.96-193453.4: WISE J1820+. The last two stars are referred to as WISE-ToI-222 and WISE-ToI-223 in Karambelkar et al. (2021); Tisserand et al. (2020).

Table 2. Adopted stellar parameters.

Name	T_{eff} (K)[a]	$\log g$ (cm s^{-1})	ξ (km s^{-1})	v_{mac} (km s^{-1})
HD 137613	5500[b]	1.0	6.5	0.0
HD 182040	5750	1.0	6.0	0.0
A223	6250	1.0	7.0	0.0
B566	5750	1.0	6.0	0.0
B42	5500	1.0	6.0	0.0
C38	5750	1.0	6.0	0.0
AO Her	4750[b]	1.0	7.0	8.0
ASAS-RCB-18	5000	1.0	7.0	6.0
ASAS-RCB-21	5000[b]	1.0	7.0	8.0
NSV 11154	5250	1.0	6.0	8.0
WISE J1818+	5000	1.0	7.0	8.0
WISE J1942+	4500[b]	1.0	7.0	6.0

[a] Chosen values are the nearest available from our grid of models. Values without a source in literature are adopted using empirical color-temperature calibration (Crawford et al. 2023)
[b] References: Tisserand (2012), Bergeat et al. (2001), Karambelkar et al. (2021)

Species	Wavelengths (μm)
S I	2.2655, 2.2707, 2.2875
Si I	2.2665, 2.275, 2.3142, 2.3953, 2.4245, 2.4575
Fe I	2.262, 2.277, 2.2835, 2.331, 2.4164, 2.4265
Na I	2.3348, 2.338
Mg I	2.2808, 2.2906
C I	2.2642, 2.2685, 2.3436, 2.3443, 2.3613, 2.3736
$^{12}C^{16}O$	2.293, 2.322, 2.352, 2.382, 2.414, 2.445, 2.478
$^{12}C^{18}O$	2.349, 2.378, 2.408, 2.438, 2.469

Table 3. Locations of prominent features in our spectra.

sistent with the DD scenario and other observations of HdC stars (Clayton et al. 2007; Jeffery et al. 2011). We also searched for 1 – 0 lines of HF which were recently detected in the K-band spectrum of DY Per (García-Hernández et al. 2023) but found none. García-Hernández et al. (2023) also did not observe these lines in the RCB WX CrA and other HdC stars, and note that the absence of HF lines is likely indicative of a severe H-deficiency rather than a F-deficiency in these stars, as the abundances of both affect the formation of HF in the atmosphere.

3.2. Possible CO Emission Line Contamination

We note that for the RCB stars in our sample, strong $^{12}C^{16}O$ absorption lines beyond 2.35 μm appear flattened or distorted. While the wings of these lines match the profiles of model synthetic spectra, the cores appear truncated. This is seen in all RCBs in our sample (most prominently in ASAS-RCB-21) but in none of the dLHdCs. This truncation is most noticeable at strong $^{12}C^{16}O$ absorption bandheads and gets more pronounced towards redder wavelengths. Figure 3 compares prominent $^{12}C^{16}O$ bandheads in ASAS-RCB-21 and HD 137613, illustrating clear distortions from the synthetic spectrum in the RCB star, while the dLHdC shows a near-perfect match with the synthetic spectrum.

Dilution of absorption bands due to circumstellar dust is unlikely to explain this as nearby absorption lines of similar strength around the truncated CO bandhead are unaffected. We expect dilution to uniformly weaken the spectra of RCB stars, and this is discussed in Section 3.5.2. Instead, we suggest that this truncation is due to the absorption lines being 'filled out' by CO emission lines from circumstellar molecular gas around the RCB stars. Narrow emission from circumstellar C_2 and CN molecules has been previously detected in RCB stars (Kameswara Rao et al. 1999, 2004) during the decline phase. This circumstellar emission is believed to be persistent (Kameswara Rao et al. 2004), and can contaminate photospheric absorption lines even if the star is

observed at maximum light. We expect the strongest lines to be the most affected, as their corresponding circumstellar emission lines would also be strong – this explains the severity at bandheads. Conversely, weak lines are unaffected. We have had some success in replicating such line profiles with a toy model that combines CO emission lines obtained by inverting an absorption spectrum, confirming that this is a plausible explanation.

It is important to emphasize that this does not seem to affect the entire spectrum. We note that lines of the 2 – 0 and 3 – 1 bandheads are unaffected, while the subsequent bandheads (λ > 2.35 μm) show progressively more severe effects at redder wavelengths. This could be related to how energy levels are populated by collisional excitation, and is an interesting avenue for future studies. We exclude such lines from our analysis and they do not affect our abundance measurements.

3.3. Spectral Modeling

We constructed model synthetic spectra using a grid of hydrogen-deficient, spherically symmetric MARCS (Model Atmospheres in Radiative and Convective Scheme) atmospheric models, generated with input abundances of $\log \epsilon(H) = 7.5$, $\log \epsilon(He) = 11.5$, $\log \epsilon(C) = 9.5$ (C/He = 0.01), and $\log \epsilon(O) = 8.8$ (Gustafsson et al. 1975, 2008; Bell et al. 1976; Plez 2008). The models were constructed for five different nitrogen abundance values of $\log \epsilon(N) = 7.0$, 7.5, 8.0, 8.5, and 9.4[2]. A solar metallicity is assumed for other elements. The models assume a stellar mass of 1 $M_\odot$, surface gravity values ($\log g$) = 1.0, microturbulence (ξ) = 5 km s^{-1}, and were computed for a grid of effective temperatures (T_{eff}) ranging from 4000 – 7500 K (in steps of 250 K).

We generated synthetic spectra using TSFitPy (Storm & Bergemann 2023) – a python wrapper around the radiative transfer package Turbospectrum v20.0 (Alvarez & Plez 1998; Plez 2012; Gerber et al. 2023). We used the CO line list provided by B. Plez (priv. commun. and described in Goorvitch (1994)) and the ExoMol linelists for CN and C_2 (Yurchenko et al. 2018; Tennyson et al. 2024). Atomic line lists are generated using the VALD database (Ryabchikova et al. 2015).

3.4. Spectral Fitting

We fit the models to our observed spectra to derive the abundances of different elements. In addition to the ele-

---

[2] Note: $\log \epsilon(X)$ refers to abundances normalized to $\log \sum_i \mu_i \epsilon_i = 12.15$, where μ_i is the mean atomic weight of the element i. This will be denoted by $A(X)$ throughout the text.
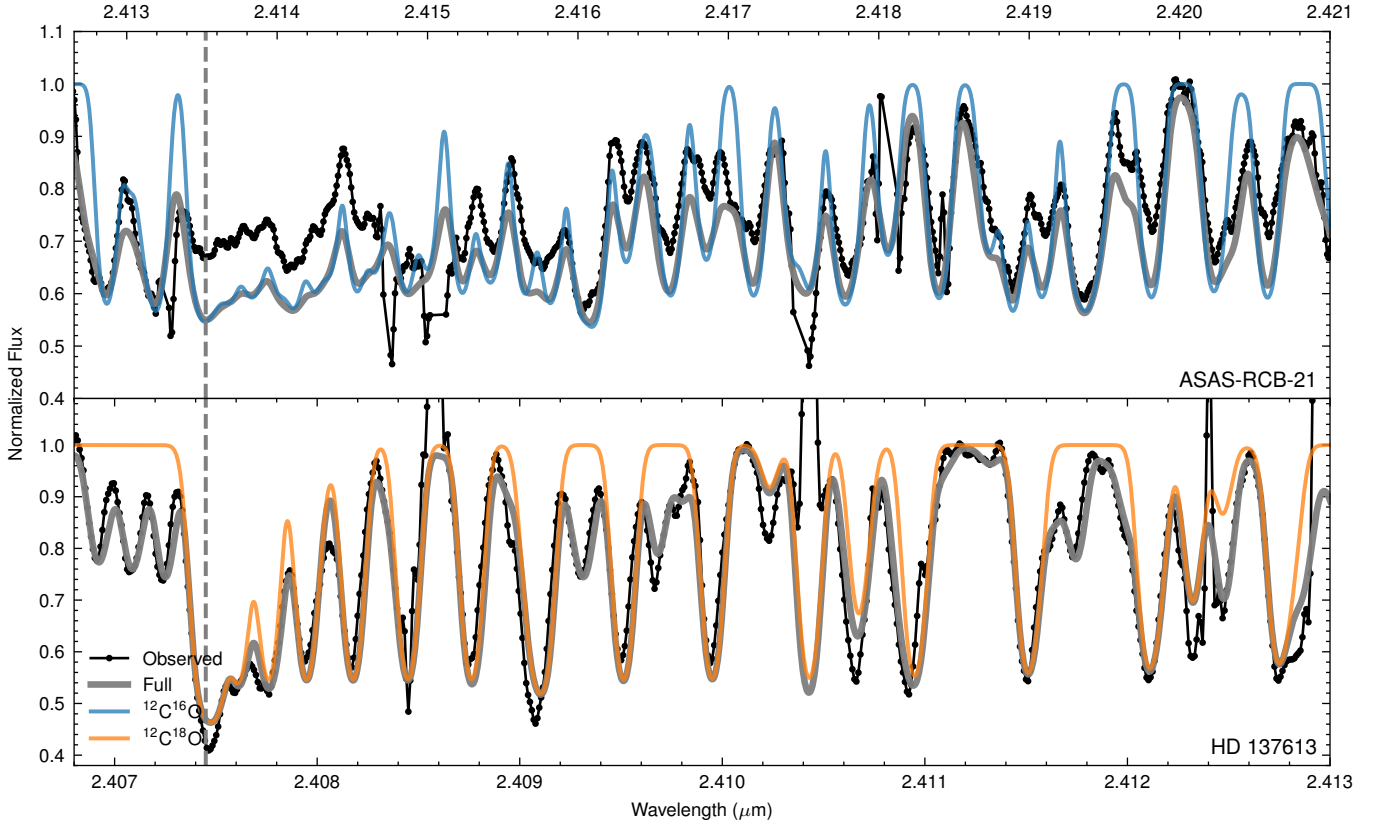
Figure 3. A comparison of strong bandhead of $^{12}C^{16}O$ (ASAS-RCB-21, top) and $^{12}C^{18}O$ (HD 137613, bottom) highlighting the distortions of stronger lines observed in RCB stars, likely due to contamination from circumstellar emission lines (see Section 3.2). The location of the respective bandheads is indicated by a dashed vertical line.

mental abundances, the model fitting requires four additional stellar parameters – effective temperature ($T_{\rm eff}$), surface gravity ($\log g$), microturbulence (ξ), and macroturbulence ($v_{\rm mac}$). The micro- and macroturbulence velocities are free parameters in our fitting and are estimated using the observed spectra (see below for details). We fix $\log g = 1.0$ for all stars, and use estimates of $T_{\rm eff}$ from literature where available. Table 2 lists the stellar parameters adopted for the stars analyzed here.

We convolve the synthetic spectra with a Gaussian function to match the iShell spectral resolution and fit the convolved models to our observed spectra using χ^2 minimization implemented in `TSFitPy`. We made some modifications to the default version of `TSFitPy` to include the synthetic spectra generated from our custom, sparse model grid. Specifically, we suppressed the interpolation of metallicity, $\log g$, and $T_{\rm eff}$. We also modified the code to use $^{16}O/^{18}O$ ratio as a free parameter for fitting.

The carbon, nitrogen, oxygen abundances and oxygen isotope ratios for each star in our sample are derived using the following steps (illustrated in Figure 4 for HD 137613) –

1. An inital guess for the different elemental abundances is obtained by visually comparing the models with the observed lines.

2. The microturbulence (ξ) is determined using the method outined in Magain (1984). A set of single, unblended CN lines (or CO lines if a star has low $A(N)$) is identified. Models are fit to these lines to measure N (or O) abundances assuming different values of ξ. The value of ξ for which the slope between the derived abundances and the line equivalent widths is closest to zero is adopted as the microturbulence value for the star (see Figure 4(a)).

3. Clusters of partially blended lines are used to determine $v_{\rm mac}$, as the profiles of such regions show the most prominent effects of any additional broadening. We find that dLHdC stars do not show any broadening beyond instrumental resolution, while RCB stars indicate $v_{\rm mac} \sim 6 - 8$ km s^{-1}. This is illustrated in Figure 4(b) for the RCB star WISE J1818+.
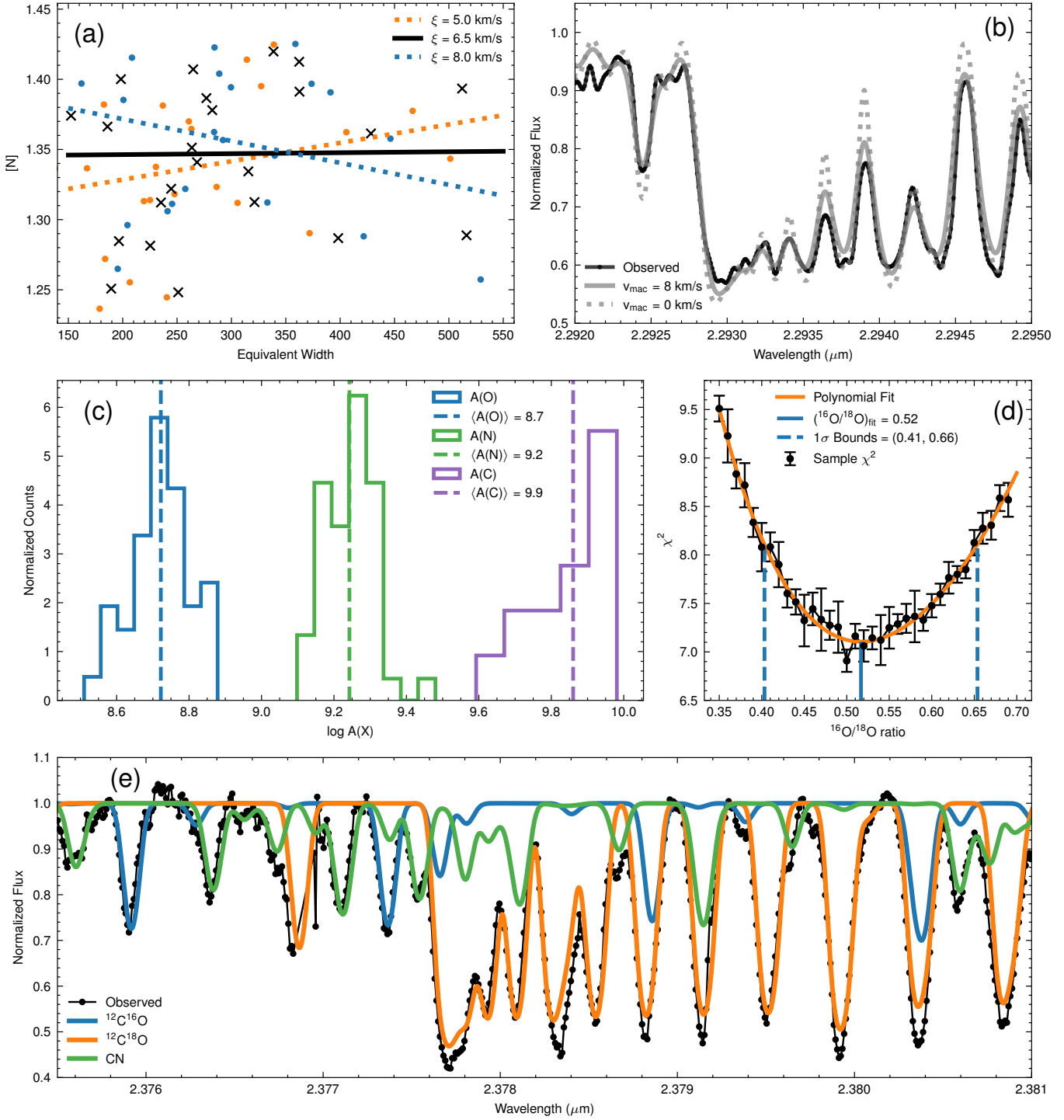
Figure 4. These panels show the steps discussed in Section 3.4 for HD 137613, except (b) which shows the cooler star, WISE J1818+ to better illustrate the $A(C)$ discrepancy.

(a) Equivalent Width v/s [N] obtained for 3 different ξ values, color-coded as per the legend with linear fits made to visually illustrate that the quantities are uncorrelated at the best-fit $\xi = 6.5$ km/s.

(b) The spectrum of RCB WISE J1818+ near the 2-0 $^{12}C^{16}O$ bandhead compared with synthetic spectra generated for a v_{mac} of 0 and 8 km/s, indicating the presence of additional broadening.

(c) Distributions of fits obtained for $A(O)$ and $A(N)$ from the respective linemasks, with mean values marked.

(d) χ^2 curve obtained by fitting a range of $^{16}O/^{18}O$ ratios, with the best-fit value and 1σ bounds marked. The χ^2 values have errorbars as the final fits have an inherent spread caused by random sampling of initial guesses.

(e) Synthetic spectra generated for individual molecules compared with the observed data, indicating they are in agreement.

4. Next, $A(C)$ is measured using 3 – 4 unblended C_2 lines that are available in our spectra. Since the vast majority of C_2 lines happen to be blended with CN, this serves as an initial estimate.

5. The obtained $A(C)$ value is then used to fit a set of 30 – 40 CN lines to measure the nitrogen abundance. This is then fed back to a larger C_2 linemask which includes blended lines to further improve the C abundance. If required, this process is iterated a few times until the derived values converge. The uncertainty on the C and N abundances is obtained by measuring the standard deviation of the line-to-line scatter in the measured abundances. Figure 4 (c) shows the distributions of fitted abundances obtained for C, N, and O.

6. Finally, the oxygen abundance and isotope ratios are measured using a set of good $^{12}C^{16}O$ and $^{12}C^{18}O$ lines. To measure the oxygen-isotope ratios, we first measure a goodness-of-fit (χ^2) by fitting synthetic spectra to all selected absorption lines simultaneously, with $^{16}O/^{18}O$ and total oxygen abundance as free parameters, and $A(C)$ and $A(N)$ set to the values determined in the previous step. We then fit a 4$^{\text{th}}$ order polynomial to the χ^2 vs $^{16}O/^{18}O$ curve to determine the best-fit $^{16}O/^{18}O$ value as the one with the minimum χ^2, and 1σ uncertainties on this using the $\Delta\chi^2 = 1$ criterion (see Fig. 4 d). We then fix the $^{16}O/^{18}O$ ratio to its best-fit value, and measure the total oxygen abundance $A(O)$ by fitting the CO absorption lines individually, similar to the measurement of C and N abundances (see Fig. 4c). We report the mean and the standard-deviation of the measured line-by-line total oxygen abundances.

Figure 4(e) shows the final fits for individual molecules.

This process yields the abundances of nitrogen, oxygen, and the oxygen isotope ratio for each star in our sample, along with 1σ uncertainties for each quantity. Additionally, the atomic lines listed in Table 3.1 are used to obtain the abundances of Fe, Mg, Na, Ca, S, and Si. However, we are unable to measure accurate uncertainties for these elements because of the small number of their unblended absorption lines in our spectra. Based on the uncertainties for the CNO elements, we conservatively estimate an uncertainty of ≈ 0.2 dex on the abundances of these elements.

The measured elemental abundances and oxygen isotope ratios for the stars in our sample are listed in Table 4. The CNO abundances and oxygen isotope ratios are precisely constrained for all stars in our sample, except WISE J1942+. For this star, the $^{12}C^{18}O$ lines are very weak compared to the $^{12}C^{16}O$ lines. This causes the χ^2 vs $^{16}O/^{18}O$ curve to flatten for large oxygen isotope ratios and never rises above the $\Delta\chi^2 = 1$ level from its minimum point. As a result, while we can measure the best-fit and 1-σ lower bound, the upper-bound on the $^{16}O/^{18}O$ is not constrained, and we report an upper limit of 500 for this star.

We obtain consistent isotope ratio measurements for the two stars HD 137613 and HD 182040 that were analyzed previously using high-resolution spectra by García-Hernández et al. (2009). The CNO abundances are slightly different because the previous study used a fixed model abundance of $A(C) = 9.5$, while we fit this using C_2 lines. Medium-resolution spectra of all six dL-HdC stars and three RCB stars in our sample were analyzed by Karambelkar et al. (2021). The isotope ratios of three of the dLHdCs and one of the RCBs are within the ranges reported from medium-resolution spectra, while the remaining ones are outside the ranges but consistent to a factor of few. The reported nitrogen abundances also have uncertainties spanning 2.5 dex in most cases. This highlights the importance of using high-resolution spectra to accurately measure abundances and isotope ratios in the K-band due to extensive blending of molecular features.

Figure 6 compares the abundances of all elements to the iron abundances, with all values relative to solar abundances. A detailed analysis of these results will be presented in a future work.

3.5. Sources of systematic errors

We now discuss the limitations of our analysis that are likely to introduce some systematic effects in the derived elemental abundances. We note that as these limitations have similar effects on the strengths of $^{12}C^{16}O$ and $^{12}C^{18}O$ lines, they should not significantly alter the oxygen isotope ratios which are the main focus of our work.

3.5.1. Model Grid

The sparse grid of H-deficient stellar models available in the literature is a significant limitation in any elemental abundance study of HdC stars. It is clear that the range of input elemental abundances available in the model-grid are not suitable for fitting the spectra of all HdC stars in our sample. For several stars, the derived abundances differ substantially from the input values assumed in the MARCS models. We cannot quantify the

Table 4. Chemical abundances and oxygen isotope ratios for the stars in our sample.

Star	$T_{\rm eff}$(K)	A(C)	A(N)	A(O)	$^{16}O/^{18}O$	[Fe]	[Mg]	[Na]	[Ca]	[S]	[Si]
HD 137613	5500	9.86 ± 0.12	9.24 ± 0.06	8.72 ± 0.08	$0.52^{+0.14}_{-0.11}$	-0.2	0.4	0.3	-0.2	-0.2	-0.4
HD 182040	5750	9.90 ± 0.13	9.08 ± 0.08	7.99 ± 0.06	$0.58^{+0.35}_{-0.24}$	-0.5	0.2	-0.0	-0.4	-0.2	-0.2
B566	5750	10.03 ± 0.25	9.09 ± 0.10	8.55 ± 0.10	$0.78^{+0.32}_{-0.23}$	-0.3	0.0	0.0	-0.5	-0.1	0.3
C38	5750	10.32 ± 0.16	9.47 ± 0.08	8.99 ± 0.10	$0.73^{+0.26}_{-0.21}$	0.2	0.7	0.6	0.0	0.2	0.2
A223	6250	9.48 ± 0.24	8.73 ± 0.09	8.20 ± 0.09	$0.60^{+0.24}_{-0.19}$	-0.8	-0.1	-0.1	-0.8	-0.4	-0.7
B42	5500	10.17 ± 0.14	9.18 ± 0.14	8.81 ± 0.1	$0.32^{+0.28}_{-0.15}$	-0.3	0.3	0.3	0.1	-0.1	0.0
NSV11154	5250	8.90 ± 0.06	7.45 ± 0.15	7.19 ± 0.10	$7.18^{+6.38}_{-2.76}$	-0.8	-1.2	-1.6	-1.5	-0.1	-0.8
ASAS-RCB-21	5000	8.86 ± 0.06	7.74 ± 0.09	7.77 ± 0.16	$6.85^{+2.30}_{-1.77}$	-0.9	-1.4	-1.2	-1.1	-0.6	-1.1
ASAS-RCB-18	5000	9.15 ± 0.05	7.83 ± 0.19	8.01 ± 0.14	$9.73^{+4.89}_{-3.02}$	-0.7	-1.2	-1.0	-0.9	-0.9	-0.4
WISE J1818+	5000	8.93 ± 0.06	7.60 ± 0.12	7.55 ± 0.10	$7.47^{+4.27}_{-2.73}$	-0.7	-1.3	-1.3	-0.9	-0.2	-1.0
AO Her	4750	8.95 ± 0.05	6.95 ± 0.11	7.76 ± 0.14	69^{+228}_{-35}	-1.0	-1.3	-1.5	-1.7	-0.3	-0.1
WISE J1942+	4500	8.72 ± 0.06	6.59 ± 0.13	7.42 ± 0.10	93^{+500}_{-55}	-0.9	-1.2	-1.8	-1.6	0.0	-0.6

Note: Fe, Mg, Na, Ca, S, and Si abundances are reported relative to solar values of A(Fe) = 7.5, A(Mg) = 7.6, A(Na) = 6.3, A(Ca) = 6.4, A(S) = 7.2, A(Si) = 7.6, taken from Magg et al. (2022).

inaccuracies introduced by these deviations. A new set of HdC atmospheric models that span a wider range of elemental abundances is required to address this issue. The abundances derived in this paper will inform the input abundance choices for the new models.

The MARCS models used in our analysis were made with a fixed $A(C)$ value of 9.5 that appears to be too high for the cooler RCB stars in our sample. We find that $A(C)$ ranges from 8.7 to 10.3. Similarly, $A(O)$ is observed to range from 7.2 in the RCB NSV11154 to 9.0 in the dLHdC C38, and the mean value of 8.1 indicates that the fixed input model $A(O)$ of 8.8 is too large for most stars. The nitrogen abundances observed are well represented by the grid of models available in $A(N)$, and our work highlights the importance of generating a similar grid of models for $A(C)$ and $A(O)$. These discrepancies from the input model abundances are likely to introduce errors in the absolute abundances we report.

Our analysis of the limited number of Fe lines available in our spectra also hints at differences between the metallicity of the two classes, with the mean [Fe] = −0.3 for dLHdC stars and [Fe] = −0.8 for RCB stars. It is clear that the assumed solar metallicity in the MARCS models is not appropriate for most of these stars, and an expansion of the model grid to include sub-solar metallicities is necessary.

3.5.2. Dust Dilution

RCB stars show an infrared (IR) excess due to the presence of warm circumstellar dust (Feast et al. 1997; García-Hernández et al. 2009; Tisserand 2012). This is expected to contribute an additional continuum flux component that has a veiling effect over photospheric

absorption lines, resulting in the lines appearing weaker than they actually are. This effect is evident in the spectrum of the IRAS 1813+ shown in Figures 1 and 2. As discussed in Section 2, this star was in a decline of $\Delta V \approx 1$ mag from its maximum luminosity, indicating that a fresh dust ejection episode from this star has severely diluted the photospheric spectrum. This phenomenon is also expected to weaken the lines of the other RCB stars in our sample by a lesser extent, but this is an effect that we are unable to correct for. It is likely that the derived absolute abundances for these stars are slightly underestimated due to this effect, but the oxygen isotope ratios should be unaffected.

3.5.3. Stellar Parameters

Table 5 lists the errors introduced by small changes in the input parameters of the models. We checked the effects of changing $T_{\rm eff}$, $\log g$, $v_{\rm mic}$, and $v_{\rm mac}$ on the derived abundances for the star ASAS-RCB-21. Based on these results, we add a systematic uncertainty of 0.15 dex, 0.2 dex, and 0.1 dex to the nitrogen, oxygen, and carbon abundances respectively, and xx to the oxygen isotope ratio.

3.5.4. Carbon Problem

One main issue encountered while studying HdC stars' atmosphere is the so-called 'carbon problem' that was extensively discussed by Asplund et al. (2000) in their detailed analyses of high-resolution optical spectra of warm ($T_{eff} > 6250$ K) RCB stars. The issue arises because the photoionization of neutral carbon atoms, that are in a highly excited states in such warm atmospheres, is the dominant source of continuous opacity. This leads to a discrepancy between the predicted and the observed

Table 5. Effect of changes in the input stellar parameters on the derived abundances of ASAS-RCB-21.

	Chosen Value	Δ(param)	$\Delta A(N)$	$\Delta A(O)$	$\Delta A(C)$	$\Delta\,^{16}\mathrm{O}/^{18}\mathrm{O}$
T_{eff}	5000 K	± 250 K	± 0.12	± 0.05	± 0.07	
$\log g$	1 cm s^{-2}	-0.5 cm s^{-2}	-0.03	-0.15	± 0.03	
v_{mic}	7 km s^{-1}	± 2 km s^{-1}	± 0.05	± 0.18	± 0.05	
v_{mac}	8 km s^{-1}	± 2 km s^{-1}				

C I lines strength. The carbon abundances derived from C I absorption lines are systematically lower by a median value of ∼0.6 dex than the input abundances in the stellar atmospheric models (Asplund et al. 2000).

To get around the 'carbon problem', Hema et al. (2012, 2017) used the C_2 lines to measure the carbon abundance from their optical high resolution spectra. This technique appeared to be an excellent alternative. However the measures with C_2 lines resulted in values systematically lower than the ones found with C I lines, implying that the ratio C/He in HdC stars' atmosphere should be much lower that the ratio of ∼0.6% measured in EHe stars (Asplund et al. 2000; Pandey et al. 2006). Consequently, they noted that, if one considers that both groups of stars should have similar modes of formation, a version of the carbon problem with the C_2 lines could also affect their measurements. Overall, using warm and cold HdC stars, they estimated that the carbon abundance should be lower for all HdC stars, and extrapolated low C/He ratios ranging between 0.03% and 0.3%. Furthermore, it is worth noting that, with their colder HdC stars sample, their measure of the carbon abundance from the C I lines and from the C_2 lines agreed (their Table 6), indicating possibly a variation of the 'carbon problem' with effective temperature.

García-Hernández et al. (2010) underlined that, depending of the HdC star effective temperature, the main contributor to the continuous opacity may change to free-free absorption from neutral helium when observing in the infrared K band, thus the 'carbon problem' could disappear at such wavelength. García-Hernández et al. (2009, 2010) measured the carbon abundance for 5 cold RCB, 2 cold dLHdC and 2 warm dLHdC (T$_{eff}$ > 6250 K) stars from high resolution infrared spectra. Using the unblended C I line at 2.3438 μm for the cold HdC stars and adding the nearby 2.3443 μm C I line for the warm HdC stars, they reported not seeing the 'carbon problem'. Their measured carbon abundances were consistent with the input model (C/He=1%), within a range of -0.3 to +0.4 dex. However, they observed a 'carbon problem' with the cold HdC stars using the C_2 lines. Their measured carbon abundance was about 0.8 dex higher than the input abundance.

Similar to García-Hernández et al. (2009, 2010), we observed cold HdC stars in the infrared. We used the new C_2 ExoMol linelist (Yurchenko et al. 2018) to estimate the carbon abundances from C_2 lines. For RCB stars, our derived C abundances range between 8.7 and 9.2, which is ∼0.6 dex lower than the input abundance of 9.52 (C/He=1%). However, conversely, for dLHdCs, our measured C abundances exceed the input abundance by 0.4 to 0.8 dex, which is similar to the result reported by García-Hernández et al. (2009). For the two dLHdC stars we have in common, HD 137613 and HD 182040, we derived a C_2 based carbon abundance that is about 0.5 dex lower than the one reported by García-Hernández et al. (2009). That is possibly explained by the use of different C_2 line lists.

The difference in C/He ratio we are observing between the RCB stars and the dLHdC stars may be related to a difference in the formation scenario. Both of them are expected to originate from WD mergers, but accumulating evidences show that RCB and dLHdC stars could be formed by different WD systems in term of total mass and mass ratios (Tisserand et al. 2022; Crawford et al. 2024).

An expanded set of models with a grid of input carbon abundances is required to quantify the extent of the carbon problem with C_2 lines. As the main focus of our study is oxygen isotope ratios, we leave this analysis for a future study and report the carbon abundances derived with our current models in Table 4.

4. DISCUSSION

4.1. *Oxygen Isotope ratios*

The main goal of this paper was to measure precise oxygen isotope ratios for a large sample of RCB and dLHdC stars. Using our high-resolution spectra, we find that all dLHdC stars in our sample have oxygen isotope ratios lower by an order of magnitude than all RCB stars in our sample. All dLHdC stars in our sample have $^{16}\mathrm{O}/^{18}\mathrm{O} < 1$, while all RCB stars have $^{16}\mathrm{O}/^{18}\mathrm{O} > 4$. The coolest star in our sample RCB WISE J1942+ has a ratio as high as 92. Our results robustly confirm that dLHdC stars tend to have lower $^{16}\mathrm{O}/^{18}\mathrm{O}$ ratios than RCB stars – a trend suggested by previous analyses of medium resolution spectra (Karambelkar et al. 2022) and small samples of high-resolution spectra (García-Hernández et al. 2010). As noted previously, this difference could potentially be explained by requiring that dLHdCs and RCBs
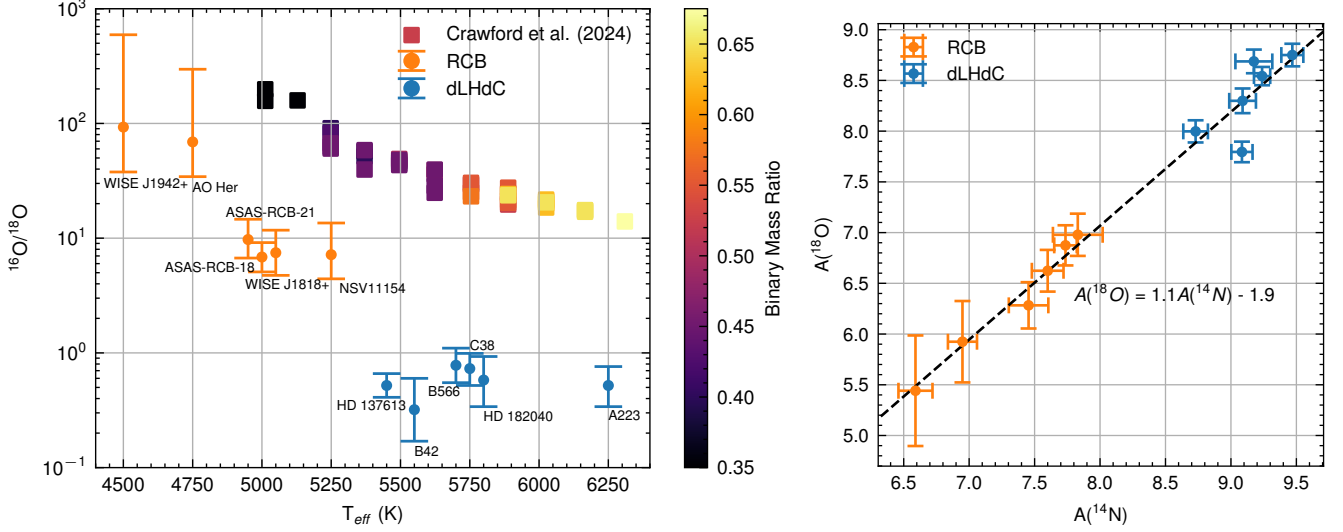
Figure 5. *Left:* Variation of oxygen isotope ratio with T_{eff} for the RCB stars (orange dots) and dLHdC stars (blue dots) in our sample. In cases where multiple stars have the same T_{eff}, offsets of 50 K have been applied for readability. We find that all RCB stars in our sample have $^{16}O/^{18}O > 4$, while dLHdC stars have $^{16}O/^{18}O < 1$. We also find a decreasing trend of the oxygen isotope ratios with effective temperature, consistent with predictions from WD merger remnant models from Crawford et al. (2024) (colored squares, color-coded by the mass-ratio of the progenitor WD binary).
Right: Abundances of ^{18}O with N (right) for the dLHdC (blue) and RCB (orange) stars in our sample. We find that $A(^{18}O)$ is linearly correlated with $A(^{14}N)$ (black dashed line), suggesting that a fixed fraction ($\approx 1\%$) of the nitrogen is converted to ^{18}O across all stars via α-capture.

originate in white-dwarf binaries with distinct properties such as total masses or mass-ratios (see Tisserand et al. 2022; Karambelkar et al. 2022; Crawford et al. 2023 for details).

Additionally, we note a correlation between the oxygen isotope ratios and the effective temperatures of HdC stars (Figure 5), with warmer stars having lower $^{16}O/^{18}O$ ratios than the cooler ones. The two coolest stars ($T_{eff} \sim 4500$ K) have oxygen-isotope ratios that are an order of magnitude larger than the warmer ($T_{eff} > 5000$ K) stars. This is the first observed trend of oxygen isotope ratios in RCB and dLHdC stars. This trend of oxygen isotope ratios with the effective temperatures of HdC stars has also been predicted by the recent Crawford et al. (2024) theoretical models. They find that the lower q ($= M_{donor}/M_{accretor}$), higher M_{tot} mergers generally produce colder stars with higher oxygen isotope ratios, while high q, low M_{tot} mergers produce hotter stars with low oxygen isotope ratios. Fig. 5 also shows the oxygen isotope ratios as a function of effective temperatures from the Crawford et al. (2024) model grid. It is promising that the models predict the same general trend seen in the observations. However, as noted in Crawford et al. (2024), the exact values of the oxygen isotope ratios are not reproduced by the models. We note that the models overpredict the observed oxygen isotope ratios of RCBs by a factor of ≈ 2.5 and dLHdCs by two orders of magnitude. Crawford et al. (2024) sug-

gest that the model oxygen isotope ratios can be reduced by adopting lower helium-shell burning temperatures (T_{SOF}), but the lowest ratio achieved for dLHdC models was 3.76, which is still significantly larger than our observations. Additionally the amount of hydrogen in the He-WD or the extent of convection can also impact the oxygen isotope ratios (Munson et al. 2021; Zhang et al. 2014). Further modeling to reproduce the observed values of the isotope ratios will shed light on the role of the WD progenitor properties (in addition to M_{tot} and q) in determining the observed properties of RCB and dLHdC stars.

We also note a positive correlation between the abundances of ^{14}N and ^{18}O in the HdC stars (Figure 5, right). This is consistent with the α-capture reaction chain $^{14}N(\alpha,\gamma)^{18}F(\beta^{+}\nu)^{18}O$ believed to be responsible for the formation of ^{18}O during partial He burning (Clayton et al. 2005). A linear fit to the data in Figure 5 (right) gives a slope of 1.1 ± 0.1 and a y-intercept of -1.9 ± 0.6 dex, suggesting that the amount of ^{18}O produced is proportional to the amount of ^{14}N present, and that $\approx 1\%$ of ^{14}N is converted to ^{18}O in all HdC stars.

5. CONCLUSION

In this paper, we have analyzed high-resolution (R≈ 75000) K-band (2.25 – 2.48 μm) spectra of six RCB and six dLHdC stars to determine their chemical abundances and oxygen isotope ratios. We fit the observed

spectra to synthetic spectra constructed using a grid of MARCS models for HdC stars and precisely measured their $^{16}O/^{18}O$ ratios. We find that all six RCB stars in our sample have $^{16}O/^{18}O > 4$ and all six dLHdC stars have $^{16}O/^{18}O < 1$, confirming previous suggestions that dLHdC stars have lower oxygen isotope ratios than RCB stars. Additionally, for the first time, we find a possible correlation between the oxygen isotope ratios and the effective temperatures of HdC stars, with colder stars having larger $^{16}O/^{18}O$ values than their hotter counterparts. This trend is consistent with recent simulations of white-dwarf mergers that explore the effects of total mass and mass ratios of WD binaries on their merger remnants. However, these models overpredict the $^{16}O/^{18}O$ values by two orders of magnitude, pointing to additional factors that could play an important role in setting the oxygen isotope ratios.

We also used our high-resolution spectra to measure abundances of C, N, O, Fe, S, Si, Mg, Na, and Ca for the twelve HdC stars. We find a linear relation between the ^{18}O abundance and the ^{14}N abundance, suggesting that a fixed fraction ($\approx 1\%$) of ^{14}N is converted by α-capture to ^{18}O in all HdC stars. We also find that all RCB stars in our sample have a lower metallicity than the dLHdC stars.

Our work highlights the need for new, publicly available MARCS models with a wider grid of input abundances to accurately model the spectra of HdC stars.

An extension to other $A(C)$, $A(O)$, and [Fe] values is necessary to successfully analyze this diverse group of stars. Additionally, all RCB stars in our sample are cooler than 5250 K, while the dLHdC stars are warmer than 5500 K. Future high resolution observations of a more diverse sample of stars will verify the trends reported in this study.

In summary, we are arriving at a consistent picture for HdC stars, where the observed differences between RCBs and dLHdCs such as their effective temperatures, luminosities, and oxygen isotope ratios can be attributed to differences in the properties of their progenitor white-dwarf binaries.

REFERENCES

Alvarez, R., & Plez, B. 1998, A&A, 330, 1109

Asplund, M., Gustafsson, B., Lambert, D. L., & Rao, N. K. 2000, A&A, 353, 287

Bell, R. A., Eriksson, K., Gustafsson, B., & Nordlund, A. 1976, A&AS, 23, 37

Bergeat, J., Knapik, A., & Rutily, B. 2001, A&A, 369, 178

Clayton, G. C. 1996, PASP, 108, 225

—. 2012, JAAVSO, 40, 539

Clayton, G. C., Geballe, T. R., Herwig, F., Fryer, C., & Asplund, M. 2007, ApJ, 662, 1220

Clayton, G. C., Herwig, F., Geballe, T. R., et al. 2005, ApJ, 623, L141

Crawford, C. L., Nikultsev, N., Clayton, G. C., et al. 2024, MNRAS, 534, 1018

Crawford, C. L., Tisserand, P., Clayton, G. C., et al. 2023, MNRAS, 521, 1674

Cushing, M. C., Vacca, W. D., & Rayner, J. T. 2004, PASP, 116, 362

Feast, M. W., Carter, B. S., Roberts, G., Marang, F., & Catchpole, R. M. 1997, MNRAS, 285, 317

García-Hernández, D. A., Hinkle, K. H., Lambert, D. L., & Eriksson, K. 2009, ApJ, 696, 1733

García-Hernández, D. A., Lambert, D. L., Kameswara Rao, N., Hinkle, K. H., & Eriksson, K. 2010, ApJ, 714, 144

García-Hernández, D. A., Rao, N. K., Lambert, D. L., et al. 2023, ApJ, 948, 15

Gerber, J. M., Magg, E., Plez, B., et al. 2023, A&A, 669, A43

Goorvitch, D. 1994, ApJS, 95, 535

Gustafsson, B., Bell, R. A., Eriksson, K., & Nordlund, A. 1975, A&A, 42, 407

Gustafsson, B., Edvardsson, B., Eriksson, K., et al. 2008, A&A, 486, 951

Hema, B. P., Pandey, G., Kamath, D., et al. 2017, PASP, 129, 104202

Hema, B. P., Pandey, G., & Lambert, D. L. 2012, ApJ, 747, 102

Jeffery, C. S., Karakas, A. I., & Saio, H. 2011, MNRAS, 414, 3599

Kameswara Rao, N., Reddy, B. E., & Lambert, D. L. 2004, MNRAS, 355, 855

Kameswara Rao, N., Lambert, D. L., Adams, M. T., et al. 1999, MNRAS, 310, 717

Karambelkar, V., Kasliwal, M. M., Tisserand, P., et al. 2022, A&A, 667, A84

Karambelkar, V. R., Kasliwal, M. M., Tisserand, P., et al. 2021, ApJ, 910, 132

—. 2024, PASP, 136, 084201

Lambert, D. L., & Rao, N. K. 1994, Journal of Astrophysics and Astronomy, 15, 47

Magain, P. 1984, A&A, 134, 189

Magg, E., Bergemann, M., Serenelli, A., et al. 2022, A&A, 661, A140

Munson, B., Chatzopoulos, E., Frank, J., et al. 2021, ApJ, 911, 103

Pandey, G., Lambert, D. L., Jeffery, C. S., & Rao, N. K. 2006, ApJ, 638, 454

Plez, B. 2008, Physica Scripta Volume T, 133, 014003

—. 2012, Turbospectrum: Code for spectral synthesis, Astrophysics Source Code Library, record ascl:1205.004

Rayner, J., Tokunaga, A., Jaffe, D., et al. 2022, PASP, 134, 015002

Ryabchikova, T., Piskunov, N., Kurucz, R. L., et al. 2015, Phys. Scr, 90, 054005

Storm, N., & Bergemann, M. 2023, MNRAS, 525, 3718

Tennyson, J., Yurchenko, S. N., Zhang, J., et al. 2024, Journal of Quantitative Spectroscopy and Radiative Transfer, 326, 109083

Tisserand, P. 2012, A&A, 539, A51

Tisserand, P., Crawford, C. L., Soon, J., et al. 2024, A&A, 684, A131

Tisserand, P., Clayton, G. C., Bessell, M. S., et al. 2020, A&A, 635, A14

Tisserand, P., Crawford, C. L., Clayton, G. C., et al. 2022, A&A, 667, A83

Vacca, W. D., Cushing, M. C., & Rayner, J. T. 2003, PASP, 115, 389

Yurchenko, S. N., Szabó, I., Pyatenko, E., & Tennyson, J. 2018, MNRAS, 480, 3397

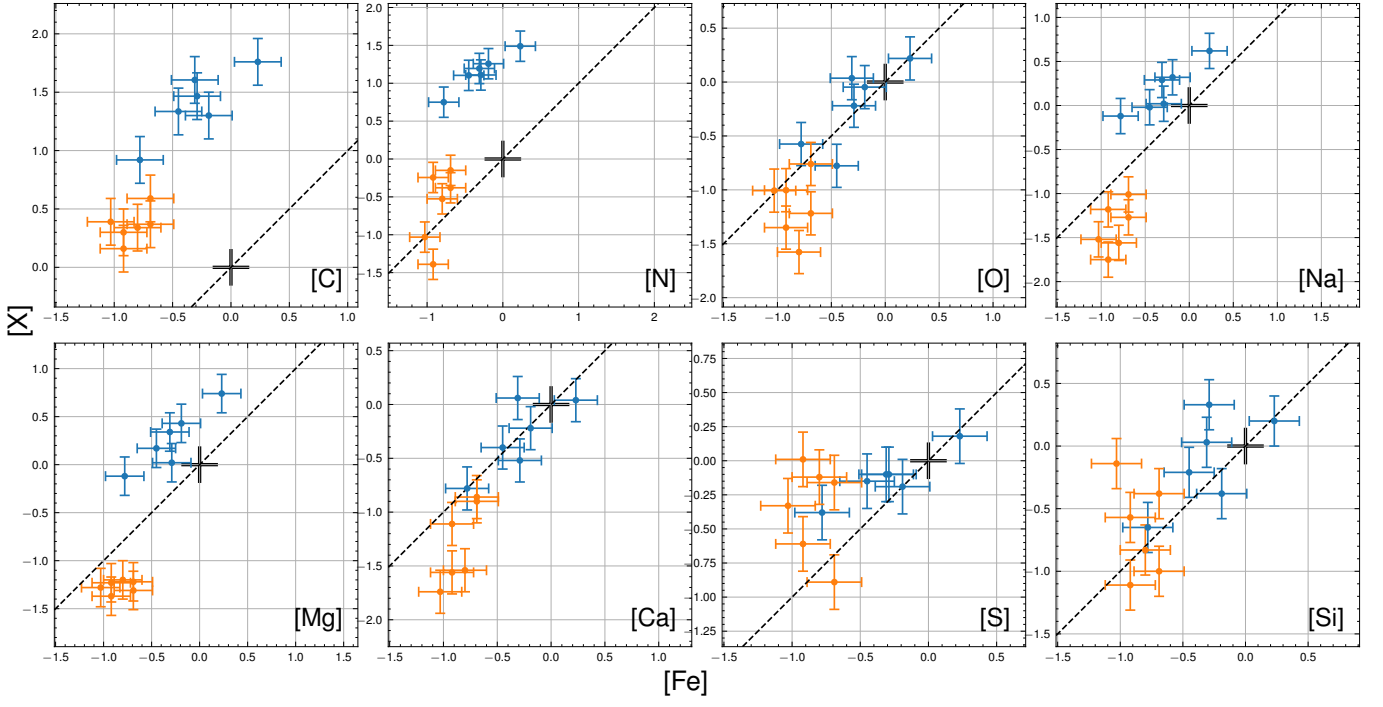Zhang, J., Wang, X., Mazzali, P. A., et al. 2014, ApJ, 797, 5

7. APPENDIX

Figure 6. Variation of other elemental abundances (y-axis) with Fe abundances (x-axis) relative to solar values for the dLHdC (blue) and RCB (orange) stars in our sample. The dashed line indicates the scaled solar abundance, and the + indicates the solar abundance for both Fe and X.